



Asthenospheric percolation of alkaline melts beneath the St. Paul region (Central Atlantic Ocean)

Daniele Brunelli^{a,b,*}, Monique Seyler^c

^a Dipartimento di Scienze della Terra, University of Modena, St. Eufemia 19, 41100, Modena, Italy

^b ISMAR-CNR, Marine Geology, Via Gobetti 101, 40129, Bologna, Italy

^c UMR 8157 CNRS - UFR Sciences de la Terre, Bât. SN5, Université des Sciences et Technologies de Lille, 59655 Villeneuve d'Ascq, France

ARTICLE INFO

Article history:

Received 4 June 2009

Received in revised form 10 November 2009

Accepted 11 November 2009

Available online 30 December 2009

Editor: T.M. Harrison

Keywords:

alkaline MORB
melt percolation
abyssal peridotite
upper mantle
Central Atlantic Ocean

ABSTRACT

Two peridotite suites collected by submersible in the equatorial Atlantic Ocean (Hekinian et al., 2000) were studied for textures, modes, and in situ major and trace element compositions in pyroxenes. Dive SP12 runs along the immersed flank of the St. Peter and Paul Rocks islets where amphibole-bearing, ultramafic mylonites enriched in alkalis and incompatible elements are exposed (Roden et al., 1984), whereas dive SP03 sampled a small intra-transform spreading centre situated about 370 km east of the St. Peter and Paul Rocks. Both suites are characterized by undeformed, coarse-grained granular textures typical of abyssal peridotites, derived from residual mantle after ~15% melting of a DMM source, starting in the garnet stability field. Trace element modelling, textures and lack of mineral zoning indicate that the residual peridotites were percolated, reacted and refertilized by ~2.6% partially aggregated melts in the uppermost level of the melting region. This relatively large amount of refertilization is in agreement with the cold and thick lithosphere inferred by previous studies. Freezing of trapped melts occurred as the peridotite entered the conductive layer, resulting in late-stage crystallization of olivine, clinopyroxene, spinel, ± plagioclase. Chondrite-normalized REE patterns in clinopyroxenes from SP03 indicate that they last equilibrated with (ultra-) depleted partial melts. In contrast, REE concentrations in clinopyroxenes from SP12 display U and S shaped LREE-enriched patterns and the calculated compositions of the impregnating melts span the compositional range of the regional basalts, which vary from normal MORB to alkali basalt sometimes modified by chromatographic fractionation with no, or very limited, mineral reaction. Thus the mylonitic band forming the St. Peter and St. Paul Rocks ridge is not a fragment of subcontinental lithospheric mantle left behind during the opening of the Central Atlantic, nor the source of the alkaline basalts as previously suggested. Rather, dive SP12 sampled residual peridotites of normal MORB mantle that were located close to channels transporting alkali basalts. Reacted melts escaping from these channels, infiltrated, and locally equilibrated with, the peridotite matrix by ion exchange reactions. Relicts of the source of the alkaline basalts were not sampled but our study suggests that it was a component of the MORB mantle underlying the St. Paul region.

© 2009 Elsevier B.V. All rights reserved.

1. Introduction

The Central Atlantic Ocean is characterized by a large concentration of closely spaced, anomalously long fracture zones, a high ratio of peridotites to volcanics exposed on the seafloor and the occurrence of alkaline basalts along with very fertile abyssal peridotites. These features were attributed to the presence of a lithospheric mantle colder and thicker with respect to other regions of the Atlantic Ocean (Bonatti et al., 1993; Schilling et al., 1995). A mid oceanic ridge “cold spot”, similar to that known at the Australian-Antarctic Discordance

may lie in the Equatorial Atlantic, in connection to downwelling of cold, dense upper mantle as suggested by Bonatti et al., 1993. Beside, global upper mantle tomography suggests the presence of a fossil detached subducted slab beneath the Equatorial Atlantic, in agreement with plate tectonic reconstructions showing that an old subduction zone remained active for the period between 460 and 300 Ma (Maia et al., 2001; Sichel et al., 2008).

Another aspect of this region is the petrology of the islets of St. Peter and St. Paul Rocks (SPPR) which have long been recognized as unusual to the oceanic environment (Darwin, 1891). They expose high temperature, strongly mylonitized, amphibole-rich mafic and ultramafic rocks which were, at first, identified as cumulates associated with alkaline basalts (Tilley, 1947; Frey, 1970; Melson et al., 1967a,b). A trace element and isotopic study led Roden et al. (1984) to suggest a 155 Ma old metasomatic event as the origin of

* Corresponding author. Dipartimento di Scienze della Terra, University of Modena, St. Eufemia 19, 41100, Modena, Italy. Tel.: +39 059 2055815; fax: +39 059 2055898.
E-mail address: daniele.brunelli@unimore.it (D. Brunelli).

these ultramafics. At this time residual mantle peridotites dynamically recrystallized while percolated by magmatic fluids. Based on this age and on mineral compositions, [Bonatti \(1990\)](#) interpreted these rocks as representative of a subcontinental lithospheric mantle left behind after the fragmentation and opening of the Central Atlantic. This very fertile, volatile-rich, upper mantle has long been thought to be a suitable source for Atlantic island basalts ([Roden et al., 1984](#)).

In December 1997–January 1998, the region was explored with the French submersible *Nautilie* and its support ship *R/V Nadir* to investigate the mode of emplacement of the mantle peridotites and gain insight into the origin of the St. Peter and Paul massif ([Hekinian et al., 2000](#)). The data collected during this cruise show that the islets are the emerged summits of a sigmoidal ridge ([Fig. 1](#)) composed of oceanic mantle uplifted in a nearly amagmatic environment controlled by the tectonic activity of the transform ([Hekinian et al., 2000](#); [Sichel et al., 2008](#)).

In this paper, we present a petrological–geochemical study including textural observations, reconstructed modal primary compositions and in situ mineral major and trace element compositions of two peridotite suites sampled by the submersible. Dive SP12 samples were recovered at the southern, immersed slope of the St. Peter and Paul massif (Dive SP12; [Fig. 1B](#)); they are nearly undeformed, coarse-grained peridotites, assumed to represent the protolith of the ultramafic mylonites. Dive SP03 samples were taken along the wall of a small intra-transform spreading ridge about 370 km East of the St. Peter and Paul Rocks (Intra Transform Ridge A according to [Hekinian et al., 2000](#); [Fig. 1C](#)). The aim of this study is to compare St. Paul peridotites with the global set of mid-oceanic ridge peridotites, to establish what SP03 and SP12 rocks are representative of, how they relate to each other and to St. Peter and Paul Rocks mylonites, and to have some insight into the sources of the regional basalts.

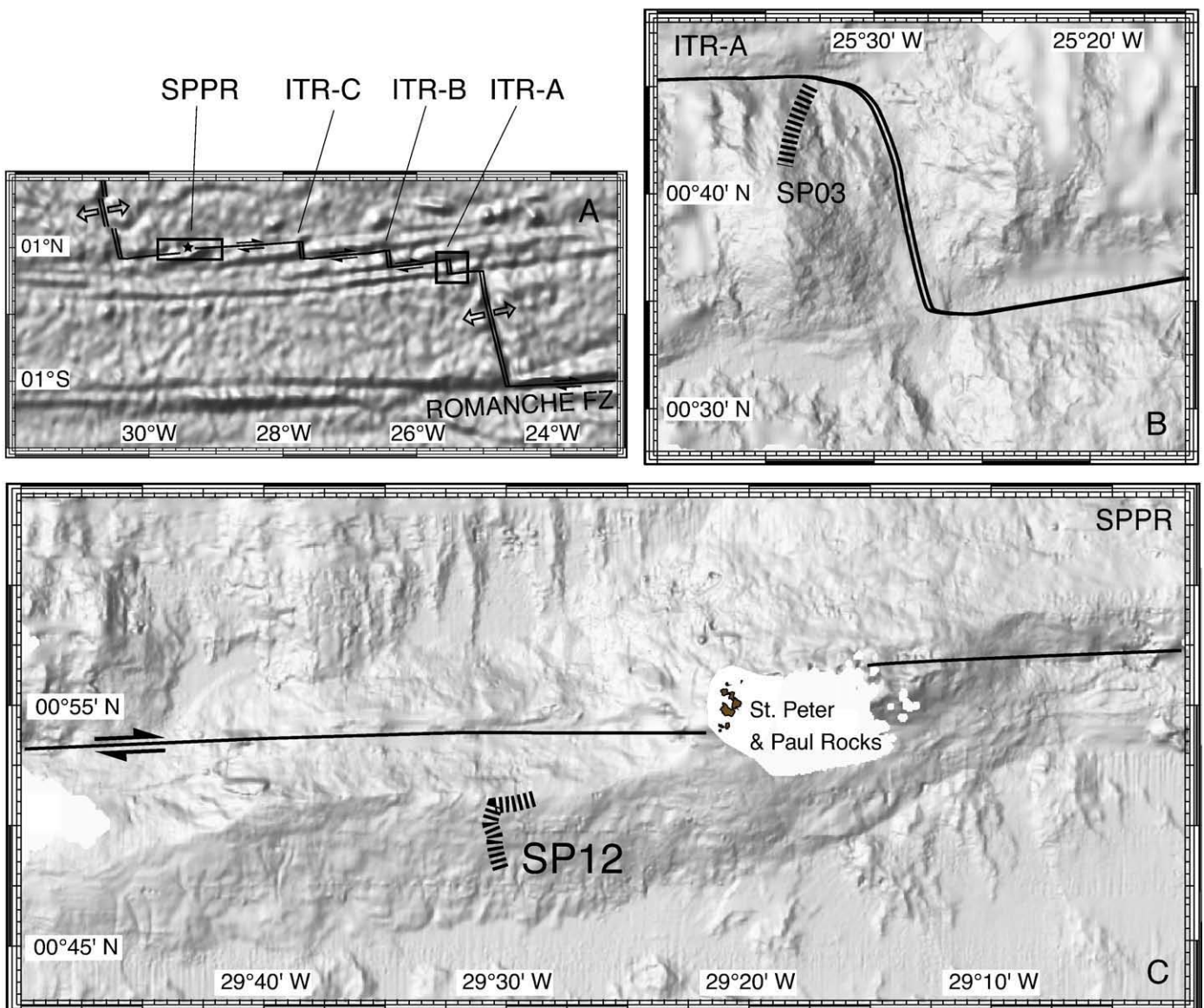


Fig. 1. Inset A: shaded relief rendering of the regional major tectonic structures based on predicted bathymetry after [Sandwell and Smith \(1997\)](#). The St. Peter and St. Paul fracture zone domain is composed of four transform faults separated by three short Intra-Transform Spreading Ridges (ITR) named according to [Hekinian et al., 2000](#). The two studied areas reported in the insets B and C are shown as boxes. Inset B: Detailed bathymetry of the Intra Transform Ridge A at 25°30' W. The trace of the *Nautilie* SP03 dive is marked on the northern slope of the inner corner high. Inset C: Detailed bathymetry of the sigmoidal ridge where the St. Peter and St. Paul rocks lie (SPPR). The trace of the principal transform displacement zone is shifted northward west of the SPPR archipelago. The trace of the *Nautilie* SP12 dive is reported on the southern flank of the ridge. Bathymetric data used in the insets B and C are from [Gasperini et al., 1997](#) and [Hekinian et al., 2000](#).

1.1. Geological setting

The St. Paul transform located at 1° N is one of the major structural discontinuities that can be traced through the entire Central Atlantic, from the Amazon basin to the coast of Liberia (Sandwell and Smith, 1997). It offsets the Mid Atlantic Ridge (MAR) by about 580 km giving an age contrast of 36 Ma (Hekinian et al., 2000). The active transform zone splits in a set of four E–W trending, en echelon, transform faults, separated by three short (10–30 km long) and deep (>4300 m) intra-transform spreading ridge segments located at 25°27' W, 26°10' W and 27°42' W, roughly oriented N 340° (Fig. 1, Hekinian et al., 2000). They show recent volcanic and tectonic activities (Schilling, 1987; Hekinian et al., 2000; Sichel et al., 2008). The St. Peter and St. Paul small archipelago is located at 29°20' W in the northernmost part of the active transform section. The detailed description of the geology of the region, as well as the exact locations and depths of sampling and preliminary results of a petrological–geochemical study can be found in Hekinian et al., 2000.

The Intra Transform Ridge-A located at 25°27' W, (Inset B, Fig. 1) was studied by means of six submersible dives near the ridge transform intersection with the southern MAR axis. This region is an example of a magma starved spreading segment, where important crustal denudation occurred during nearly amagmatic periods of lithospheric extension. The geological section drawn across the rift valley floor shows a very thin, up to 150 m thick, blanket of basalt flows and dikes covering strongly serpentinized and weathered mantle peridotites locally intruded by small gabbroic bodies (Hekinian et al., 2000). Based on the Hekinian et al., 2000 observations during dives the amount of gabbroic rocks can be estimated <15% along the Nautilé tracks. Un-sedimented fresh lavas occur on the floor of the eastern side of the rift valley, bounded by well developed fault scarps locally covered by talus breccias and slumps. Dive SP03 peridotites were collected on the northern flank of the corner high (Fig. 1B). This section consists of serpentinized peridotites intruded by small gabbroic pockets forming two continuous outcrops, on the slope of the nodal basin. Twelve peridotite samples were collected: SP03-5 and SP03-6 were taken at the base of the slope, along a ~300 m long outcrop, while SP03-10 to SP03-19 are sampled from a ~1 km long section at the top of the high (Hekinian et al., 2000). The two outcrops are separated by ~1 km of basalts. Basalts recovered in the rift valley and along its eastern wall are T- and N-MORBs.

The SPPR islets represent the emerged parts of a sigmoidal tectonic massif divided in two domains by an active E–W trending graben bounded by dolerites and floored by basalts (Hekinian et al., 2000; Fig. 1). The northern domain, to which belong the islets, is made of banded, mylonitic peridotites intruded by sporadic gabbroic bodies and associated with thin, tectonically disrupted, basaltic outcrops. The mylonites are former spinel peridotites affected by a high temperature ductile deformation that formed during sequential stages of lithospheric uplift associated with extensive E–W strike-slip motions and thrust-fault tectonics. The southern domain is fully immersed, mainly made of undeformed, serpentinized mantle peridotites with minor basalts localized in a small graben-like structure. The southern domain was also uplifted during lithospheric extension but recorded less shearing than the northern domain. Its north-facing slope exposes a mixture of carbonates, dolerites and weathered basalts, a few peridotitic mylonites and weathered massive serpentinites (Hekinian et al., 2000). Its south-facing slope exposes serpentinized ultramafic rocks, the lower part being covered by consolidated carbonate sediments. Dive SP12 peridotites were sampled in the upper part of the south-facing slope of the southern domain. Eleven peridotite samples (SP12-07 to SP12-17) were recovered from this section along a ~2 km long continuous ultramafic outcrop. Bulk rock analyses show that SP12 peridotite compositions vary from depleted to enriched in Light Rare Earth elements (LREE), but are not as enriched as the mylonites from the northern domain of the massif (Roden et al., 1984;

Hekinian et al., 2000). Basalts and gabbros from the islets are E-MORBs and alkaline in composition (Melson et al., 1972; Frey, 1970; Roden et al., 1984; Schilling et al., 1995; Hekinian et al., 2000). No mafic rocks were recovered from the southern domain (Dive SP12), but one peridotite sample contains a dykelet of clinopyroxenite with N-MORB affinity (Hekinian et al., 2000).

Based on trace element data in bulk rock peridotites, ultramafic cumulates and basalts, Hekinian et al. (2000) concluded that the various compositions of the volcanics recovered in the St. Paul area result after variable extent of melting of a lherzolitic mantle source veined with variable amounts of clinopyroxenite.

2. Sample description and petrography

Out of the 23 peridotite samples collected during dives SP03 and SP12, only seven SP03 samples and six SP12 samples are suitable for a petrological study, the others being too (>90%) serpentinized. Peridotite samples vary in size from 10 to 30 cm. All have similar, nearly undeformed, coarse-grained, granular textures, made of olivine (Ol), orthopyroxene (Opx), clinopyroxene (Cpx) and spinel (Sp). About 30% of the samples in both sets contain 1–2.5% weathered plagioclase (Pl). In both sets, samples range from lherzolite (5–6.5% Cpx) through Cpx-rich harzburgite (<5–3 vol.% Cpx) to Cpx-poor harzburgite (<3–1.5% Cpx). Modal clinopyroxene abundances show large sample-scale variability resulting in lherzolitic to harzburgitic transition at the centimetre scale. Ol/Opx/Cpx proportions plot along a trend of varying Ol/Opx ratios uncorrelated with the clinopyroxene contents (Fig. 2). Site average mineral proportions are closely similar between SP03 and SP12 (Supplementary Table 1). Textural relationships between olivine and orthopyroxene suggest that the variations of Ol/Opx ratios are caused by variable degrees of orthopyroxene dissolution and secondary olivine crystallization, as described in ODP Site 1274 harzburgites (Seyler et al., 2007; Suhr et al., 2008). However, SP03 and SP12 peridotites underwent a less extensive dissolution/precipitation process than that observed in ODP Site 1274 harzburgites where it resulted in the generation of Opx-poor harzburgites and dunites. SP03 and SP12 textural relationships are closely similar to those exhibited by normal abyssal peridotites (e.g. Seyler et al., 2001) and extremely developed in ODP Site 1274 peridotites (Seyler et al., 2007; Suhr et al., 2008). Primary olivine and orthopyroxene occurs as 1–2 cm sized grains with embayed curvilinear to lobate contacts (Supplementary Fig. 1). Orthopyroxene grains are free of plastic deformation whereas primary olivine is recrystallized into a mosaic of

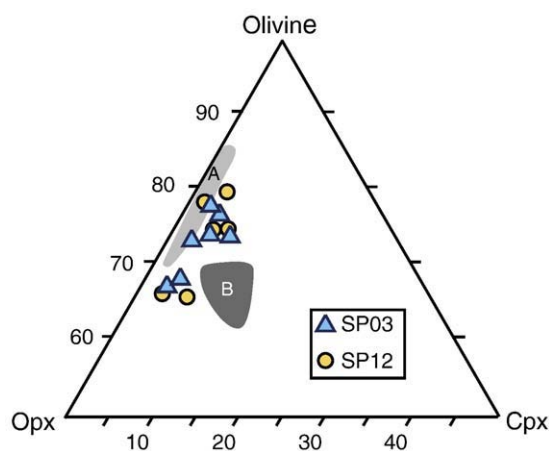


Fig. 2. Modal compositions of the SP03 and SP12 peridotites (vol.% sample average). Gray field A represents harzburgites from the 15°20' N Fracture Zone (Leg ODP 209, Seyler et al., 2007) and gray field B represents lherzolites from the Romanche Fracture Zone (Seyler and Bonatti, 1997), representing the most and least depleted abyssal peridotites of the Mid Atlantic Ridge, respectively.

3 to 4 mm sized subgrains. Coarse (>1 to 5 mm) clinopyroxene grains occur sporadically within the olivine matrix as single, isolated crystals in Cpx-poor harzburgites. In Opx-rich harzburgites and lherzolites, these large clinopyroxenes are associated in clusters, sometimes organized as elongated vein-like aggregates defining a high temperature lineation. Clinopyroxene grain boundaries in contact with olivine vary from gently curved to deeply embayed, with thin intergranular strings infiltrating far away in between olivine grains and locally relayed by small cracks filled with clinopyroxene. These intergranular extensions are characteristically associated with tiny grains of spinel and magmatic sulfides. Where in contact with each other, clinopyroxenes show straight to gently curved grain boundaries. We define as “percolative Cpx” an ensemble of small to medium-sized (up to 2 mm) clinopyroxenes characterized by microstructures which indicate crystallization from a pervasive melt percolation in a late magmatic stage. Percolative clinopyroxene (occasionally showing magmatic twins) occurs as intergranular veinlets usually associated with spinel, magmatic sulfides and secondary olivine; it often appears along orthopyroxene grain boundaries and surrounding euhedral spinel (Supplementary Fig. 1B). Late-stage clinopyroxene also fills what appears to be dissolution paths within orthopyroxene (Supplementary Fig. 1C). Spinel is rarely present as euhedral grains, usually it exhibits interstitial habit with thin intergranular extensions or appears associated with the percolative clinopyroxene or constitutes symplectites with clinopyroxene and/or orthopyroxene at the tip of the crystals. Plagioclase is heterogeneously distributed, it occurs as intergranular veinlets with or without Cr-rich Cpx ± Cr-rich Sp; it rims orthopyroxene porphyroclasts or surrounds coarse spinel grains (Supplementary Fig. 1D). Microstructures involving plagioclase are closely similar to those involving percolative clinopyroxene in the PI-free samples. One PI-bearing sample (SP03-19) contains a clinopyroxenite patch made of equant, mm-sized grains of clinopyroxene and tiny, interstitial plagioclase and Cr-rich spinel; the sample section containing this patch is referred as SP03-19b to be distinguished from the clinopyroxenite-free sample section SP03-19a.

3. Major element mineral compositions

Mineral compositions were analyzed with a CAMECA SX-100 electron microprobe at the University of Paris VI. The accelerating voltage was 15 kV and the beam current 40 nA (15 nA for Na). A 2 μm beam size was used for all minerals, except a subset of pyroxenes, for which average compositions including exsolution lamellae were obtained with a defocused beam (10–15 μm). Mineral compositions are shown in Supplementary data Tables 2–5; they vary little in individual samples, except in those containing plagioclase.

Due to extensive alteration, only few olivine grains are preserved in some SP03 samples; no fresh olivine nor orthopyroxene rims have been analyzed in samples SP12. In the SP03, olivine Mg# [= molar 100 Mg/(Mg + Fe)] and NiO contents average 90.7 ± 0.4 and $0.41 \pm 0.02\%$, respectively. Orthopyroxene Mg# averages 90.8 ± 0.2 in SP03 samples with no significant variation between core and rims, and 90.5 ± 0.2 in SP12 samples. Orthopyroxene in sample SP03-19 containing the clinopyroxenite patch is significantly enriched in Fe (Mg# ~88.5). In PI-free samples, SP03 and SP12 orthopyroxene core compositions for Al₂O₃, Cr₂O₃ and Cr# [molar 100 Cr/(Cr + Al)] are very similar (Supplementary Fig. 2, Fig. 3 and Supplementary data Table 3). Orthopyroxene rims (in SP03) have low Al₂O₃ and Cr₂O₃, typical for abyssal peridotites. Orthopyroxene in PI-bearing samples is variably impoverished in Al₂O₃ depending on its proximity to, and/or the amount of plagioclase (Supplementary Fig. 2B). Accordingly, orthopyroxene Cr# in PI-bearing samples is variable and high (14.7 ± 3.0). CaO contents, integrating thin clinopyroxene exsolution lamellae, show no significant intra- and inter-sample variations in PI-free and PI-bearing

peridotites, ($1.8 \pm 0.5\%$ in samples SP03 and $1.6 \pm 0.3\%$ in samples SP12).

In PI-free thin sections clinopyroxene composition ranges and averages do not vary significantly from sample to sample and are similar in both sample sets, except for Na₂O and TiO₂ contents (Fig. 3A, B). Overall coarse-grain cores have higher Al₂O₃ and Cr₂O₃ contents, lower CaO and lower Mg# (91.0 ± 0.5) relative to the average of the percolative clinopyroxenes. Cr#s show no core–rim variations and are nearly similar in coarse and percolative grains. Tiny interstitial clinopyroxene grains and extreme rims have more extreme compositions, down to 2.9% for Al₂O₃ and 0.8% for Cr₂O₃. Na₂O and TiO₂ have broad ranges of concentrations and are negatively correlated (Fig. 3B). Compositions of individual grains range from 0.57 to 0.34 wt.% Na₂O and from 0.21 to 0.06 wt.% TiO₂ in SP12, and from 0.47 to 0.29% Na₂O and 0.27 to 0.10 wt.% TiO₂ in SP03. Clinopyroxene in PI-bearing samples are characterized by variable Al₂O₃ contents, starting from concentrations similar to those in the cores of the coarse clinopyroxene grains in PI-free samples, and then decreasing towards the rims and in the percolative clinopyroxene. Cr₂O₃ contents increase slightly, so that Cr# is high and variable, in the 17–25 range (Fig. 3C). Na₂O and TiO₂ contents in PI-bearing SP03-11 and SP12-12 are in the ranges of the SP03 and SP12 PI-free samples, respectively, except for two analyzed intergranular veinlets which are highly enriched in TiO₂ (Fig. 3D).

At the sample scale, ortho- and clinopyroxene are in close equilibrium for Mg–Fe and Cr–Al exchange reactions as shown by Mg# and Cr# distributions between the two pyroxenes: Mg# Opx/Cpx average 0.993 ± 0.005 ; Cr# Opx/coarse-Cpx average 0.81 ± 0.08 ; Cr# Opx/percolative-Cpx average 0.75 ± 0.09 ; these ratios are similar to those observed in ordinary abyssal peridotites. In contrast, equilibrium temperatures calculated with the Opx-Cpx Ca–Mg exchange geothermometer (985 to 1150 °C; average 1073 ± 53 °C) yields lower temperature than those calculated with the Ca-in-Opx formulation (1075 to 1245 °C; average 1177 ± 54 °C). These temperatures, calculated at 1 GPa using Brey and Kohler (1990) geothermometers, are nevertheless typical of the abyssal peridotites (Agranier and Lee, 2007; Hellebrand et al., 2005).

Spinel grains in SP03 and SP12 show a large range of compositions, defining a broad, single trend (Supplementary Fig. 3). Cr# vary from 22.0 to 55.3, positively correlated with TiO₂ contents. Spinel in the PI-free samples are Ti-poor (<0.15%) and have the higher concentrations in Al and Mg. Spinel in PI-bearing samples have highly variable composition, depending of their textural position with respect to plagioclase. Such evolution from Cr–Ti-poor spinels to Cr–Ti-rich spinels associated with plagioclase is commonly explained by interaction between a percolating magma and the residual mantle at low pressure (Dick, 1989; Seyler and Bonatti, 1997). In our samples spinel grains enclosed in orthopyroxene have the lowest Cr# and TiO₂ contents. In sample SP03-19b, spinel grains in the peridotite matrix and interstitial spinel in the clinopyroxenite patch have similar compositions strongly depleted in Al and enriched in TiO₂ (0.6%), suggesting local equilibrium. In the whole sample set, spinel Cr# are well correlated with ortho- and clinopyroxene Cr#.

Due to alteration, plagioclase was only analyzed in the clinopyroxenite patch in sample SP03-19b where it has high anorthite content (An_{92–93}).

4. Trace element mineral compositions

Ortho- and clinopyroxene in six SP03 and six SP12 samples were analyzed for REEs, Zr, Ti and Sr, Y, Ba, Sc by secondary ion mass spectrometry, using an upgraded Cameca IMS-4f ion microprobe at the University of Montpellier and a Cameca IMS 4f ion microprobe, located at CNR-IGG, Pavia (Italy) following procedures described in Bottazzi et al. (1994). Within-grain variations were checked by analyzing four spots in the same clinopyroxene grain in sample SP03-

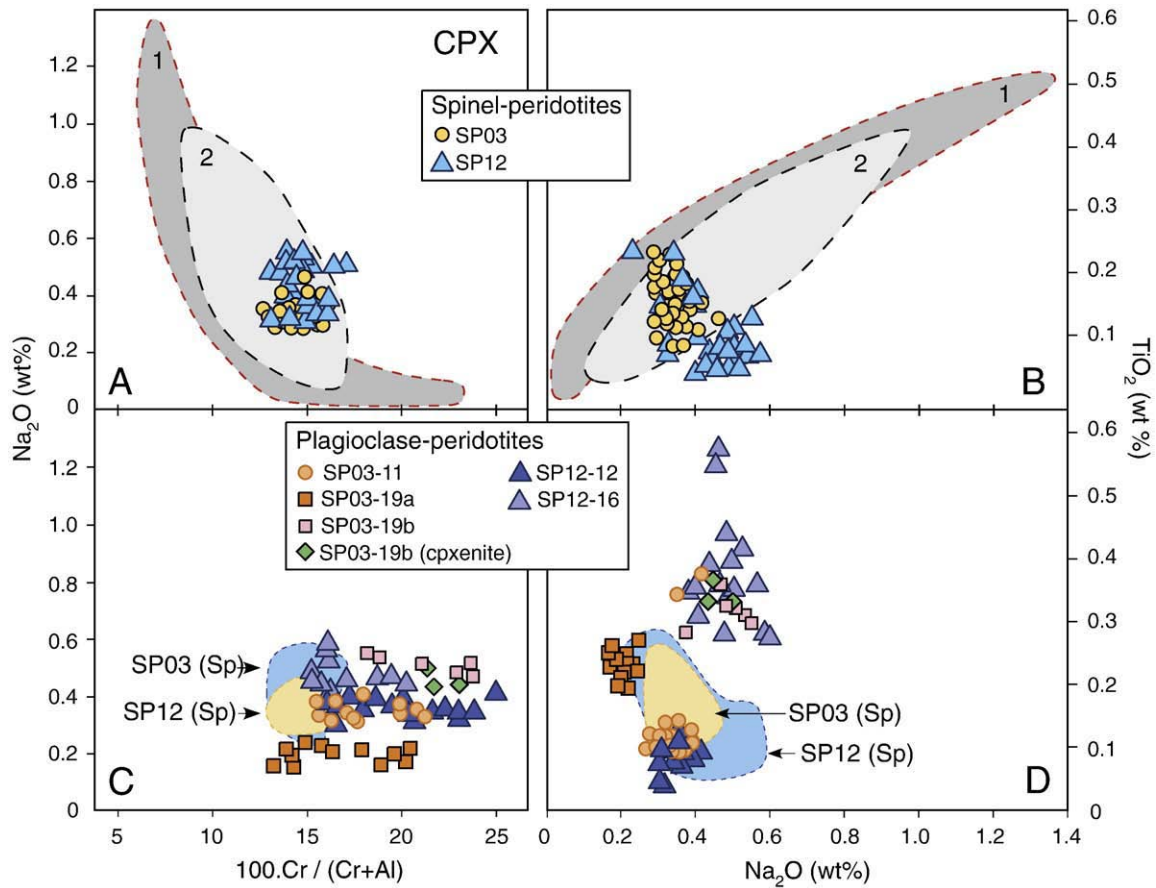


Fig. 3. Composition of clinopyroxenes of St. Paul peridotites, Sites SP03 and SP12. (A) and (B): Plagioclase-free, spinel peridotites. Fields 1 and 2 are compilations of clinopyroxenes from abyssal spinel peridotites of the Mid Atlantic Ridge and eastern Southwest Indian Ridge, respectively. (C) and (D): Plagioclase-bearing peridotites. Fields of St. Paul plagioclase-free, spinel peridotites are also represented.

12 and seven spots in the same grain in the sample SP12-07. Analyzed clinopyroxene textural types include small-sized, percolative grains (interstitial, granular veinlets and clinopyroxene in orthopyroxene corrosion paths), coarse grains (isolated and cluster-forming crystals), cores and rims; we have distinguished between curved grain boundaries filled by coarse olivine grains (noted as rims) and thin intergranular extensions within the olivine matrix (noted as percolative rims). Clinopyroxenes from PI-bearing samples (SP03-11, SP03-19, SP12-12, SP12-16, Table 1A) have been divided in low-Cr# clinopyroxene (<17), which are apparently not re-equilibrated with the nearby plagioclase (all are coarse-grain cores), and high-Cr# clinopyroxene (≥ 17), which are variably depleted in Al relative to Cr. Orthopyroxene cores (one to three spots per grain) that were analyzed have Al-rich compositions except in the PI-bearing SP12-12 sample. Results (Table 1B) show that within-grain and within-sample compositional variations are, with very few exceptions, extremely limited, with no systematic correlations with respect to grain shape, grain size and spot location within the grain (e.g. core, rim).

Low Cr# SP03 clinopyroxenes fall in a restricted compositional range (Fig. 4A), characterized by LREE-depleted Chondrite-normalized patterns [(Ce/Yb) $_N$ = 0.01–0.03] and flat HREEs varying from 5 \times to 8 \times Chondrite. Exceptions are SP03-12 (PI-free) and SP03-11 (PI-bearing) samples in which late-stage clinopyroxene display heterogeneous compositions. In SP03-12, an intergranular veinlet is LREE-enriched [(Ce/Yb) $_N$ = 0.09] with respect to the coarse clinopyroxene including its percolative rim (Table 1A). In SP03-11, the high-Cr# clinopyroxene also forming an intergranular veinlet and the low-Cr# coarse clinopyroxene have distinct REE and Sr compositions which are attributed to equilibrium with plagioclase for the former. The two analyzed SP03 high-Cr# clinopyroxene, in SP03-11 and in the SP03-19b clinopyrox-

enite patch, are enriched in REEs (Yb $_N$ = 10–13 \times Chondrite) and in LREEs [(Ce/Yb) $_N$ = 0.15–0.25] with respect to the low Cr# clinopyroxene (Table 1A). In addition, both show weak negative anomalies in Eu and strong negative anomalies in Sr with respect to Ce and Nd.

Absolute and relative REE compositions of SP12 clinopyroxenes vary very little in individual samples, but are highly variable from sample to sample (Table 1A, Fig. 4B). All SP12 clinopyroxenes have flat HREE patterns from Dy to Lu, which are 4–6 times enriched relative to Chondrite, but differ for L- and MREEs. Only in two samples, SP12-13 and SP12-16, clinopyroxenes, all low-Cr#, display classical LREE-depleted patterns [(Ce/Yb) $_N$ = 0.16 and 0.08, respectively]. SP12-16 trace element concentrations are indeed similar to those of the enriched SP03-11 intragranular grains. SP12-07 clinopyroxenes show near-flat REE patterns with a clear depletion of the light-most elements La and Ce [(Ce/Sm) $_N$ = 0.62]. The other three SP12 samples have clinopyroxenes characterized by sigmoid L- and MREE patterns. SP12-10 clinopyroxenes are strongly depleted in MREEs with an U-shaped pattern between La and Dy [(Ce/Yb) $_N$ = 0.88; (Ce/Sm) $_N$ = 2.62; (Sm/Dy) $_N$ = 0.35]. SP12-12 high Cr# clinopyroxenes are the most enriched in LREEs [(Ce/Yb) $_N$ = 2.43] with a hump in Nd (Nd $_N$ = 14 \times Chondrite); they also display strong negative anomalies in Sr consistent with their equilibration with plagioclase. Clinopyroxenes from SP12-14, characterized by very low Cr# (<14) have patterns slightly concave-upward between La and Nd, with a high in Ce [(Ce/Yb) $_N$ = 1.78], then concave-downward from Nd to Gd.

SP03 orthopyroxene REE patterns show regular decreases from the HREEs to the LREEs, with variable re-enrichments in La and Ce (Table 1B, Fig. 4B). SP12 orthopyroxene patterns vary from LREE-depleted (SP12-13 and SP12-16) to near-flat, LREE-enriched patterns (SP12-7 and SP12-12). SP12-12 orthopyroxene is equilibrated with

Table 1A
Major element compositions in wt.% of the cpx analyzed for trace elements. Each composition is an average of several analyses per grain, except for very small sized grain for which only one analyse is available. Cores and rims of same grain are reported separately.

	SP03-10		SP03-10		SP03-10		SP03-11		SP03-11		SP03-12		SP03-12		SP03-12		SP03-15		SP03-15		SP03-15		SP03-17		SP03-19a		SP03-19b		SP12-7		SP12-7	
	CIC		CPR		P		CIC		Pv		CCC		CPR		Pv		CIC		CR		P		CIC		CIC		Cpxenite		CCC		CCC	
	Ave.	±	n = 1	Ave.	±	Ave.	±	Ave.	±	Ave.	±	Ave.	±	Ave.	±	Ave.	±	Ave.	±	Ave.												
SiO ₂	50.82	0.24	50.72	0.19	51.15	0.09	50.43	0.20	51.71	0.34	51.22	0.08	50.69	0.21	51.56	51.44	0.35	51.50	0.37	51.04	0.17	51.34	0.34	50.54	0.21	52.25	0.46	50.70	0.06	50.72	0.13	
TiO ₂	0.14	0.02	0.15	0.02	0.18	0.01	0.11	0.01	0.36	0.03	0.23	0.01	0.20	0.00	0.25	0.15	0.00	0.13	0.01	0.16	0.02	0.19	0.02	0.24	0.03	0.35	0.02	0.18	0.01	0.19	0.00	
Al ₂ O ₃	5.39	0.42	5.36	0.20	5.23	0.11	5.82	0.10	4.25	0.31	5.16	0.12	5.31	0.06	5.13	5.83	0.03	5.23	0.17	5.49	0.33	5.59	0.20	5.75	0.20	2.98	0.12	5.32	0.16	5.22	0.08	
Cr ₂ O ₃	1.40	0.06	1.21	0.07	1.44	0.00	1.67	0.03	1.54	0.12	1.32	0.01	1.25	0.01	1.32	1.49	0.06	1.34	0.07	1.42	0.04	1.51	0.06	1.42	0.08	1.27	0.01	1.39	0.04	1.37	0.01	
FeO	2.94	0.19	3.07	0.28	2.78	0.32	2.85	0.06	2.90	0.45	2.95	0.01	2.78	0.06	2.66	3.16	0.39	2.97	0.10	2.73	0.10	2.95	0.08	3.32	0.21	3.40	0.07	2.97	0.10	2.99	0.06	
MnO	0.08	0.07	0.13	0.05	0.10	0.03	0.08	0.02	0.02	0.10	0.05	0.06	0.03	0.08	0.10	0.01	0.10	0.00	0.09	0.02	0.07	0.03	0.11	0.03	0.09	0.00	0.10	0.01	0.13	0.06		
MgO	16.22	0.43	16.45	0.32	16.33	0.53	15.71	0.26	17.24	1.78	17.32	0.35	15.86	0.14	16.40	17.18	1.61	16.80	0.24	15.75	0.15	16.50	0.40	16.44	0.85	17.03	0.04	16.12	0.49	15.94	0.35	
CaO	22.18	0.59	21.80	0.63	22.01	1.21	21.79	0.19	21.33	2.04	20.72	0.49	22.56	0.06	22.37	20.67	1.80	21.14	0.07	21.75	0.34	21.64	0.66	21.01	1.13	21.06	0.30	21.28	0.29	21.69	0.52	
Na ₂ O	0.31	0.01	0.31	0.03	0.39	0.01	0.35	0.03	0.37	0.05	0.30	0.01	0.29	0.01	0.37	0.34	0.04	0.32	0.02	0.42	0.03	0.35	0.01	0.21	0.03	0.43	0.01	0.40	0.01	0.39	0.02	
Total	99.48	0.30	99.21	0.09	99.60	0.32	98.81	0.37	99.72	0.28	99.30	0.31	98.99	0.13	100.14	100.35	0.47	99.57	0.87	98.87	0.45	100.14	0.51	99.04	0.34	98.85	0.82	98.43	0.42	98.61	0.10	
Mg#	90.77	0.53	90.53	0.60	91.30	0.67	90.74	0.20	91.40	0.42	91.27	0.12	91.04	0.24	91.65	90.65	0.25	90.97	0.16	91.13	0.32	90.90	0.04	89.82	0.13	89.93	0.15	90.63	0.03	90.49	0.01	
CR#	14.88	0.85	13.17	0.26	15.59	0.30	16.14	0.25	19.56	2.38	14.61	0.36	13.60	0.07	14.67	14.60	0.55	14.70	0.21	14.83	0.41	15.38	0.84	14.25	0.48	22.29	0.91	14.92	0.76	14.93	0.12	
<i>Trace element compositions in ppm</i>																																
	n = 1	n = 1	n = 1	n = 1	n = 1	n = 1	n = 3	±	n = 1	n = 1	n = 2	±	n = 1	n = 1	n = 1	n = 1	n = 1	n = 1	n = 1	n = 1	n = 1	n = 1	n = 1	n = 1	n = 1	n = 4	±	n = 1	n = 1	n = 1	n = 1	
45Sc	45.6	52.9	57.4	56.1	58.0	50.2	5.6	48.7	54.0	45.8	1.0	51.9	56.9	57.2	52.8	78.8	54.3	3.2	69.1													
48Ti	746	714	772	739	931	924	186	1072	1704	864	13	941	867	742	1102	1237	879	60	841													
88Sr	2.48	1.27	2.30	2.26	0.76	1.32	0.85	0.74	7.29	0.83	0.06	1.26	0.79	1.69	0.66	2.31	7.93	0.64	6.31													
89Y	7.61	7.65	8.64	8.97	11.66	9.55	2.20	8.81	11.79	7.52	0.02	7.95	8.21	8.32	11.34	17.11	5.49	0.39	6.12													
90Zr	0.86	0.75	1.04	1.02	4.85	1.96	0.92	1.20	3.34	0.87	0.05	1.32	0.96	0.85	1.17	11.07	2.48	0.16	2.57													
139La	0.016	0.013	0.021	0.078	0.264	0.044	0.038	0.008	0.083	0.005	0.001	0.011	0.008	0.018	0.016	0.250	0.309	0.047	0.212													
140Ce	0.084	0.038	0.116	0.128	1.109	0.063	0.037	0.035	0.421	0.035	0.004	0.043	0.027	0.067	0.054	1.217	1.562	0.205	1.625													
143Nd	0.408	0.237	0.400	0.426	1.546	0.540	0.165	0.366	1.263	0.266	0.032	0.265	0.251	0.329	0.578	2.137	1.780	0.100	2.042													
147Sm	0.352	0.331	0.337	0.396	0.798	0.549	0.128	0.395	0.960	0.320	0.013	0.320	0.292	0.305	0.585	1.202	0.564	0.062	0.668													
151Eu	0.187	0.158	0.168	0.169	0.249	0.224	0.069	0.220	0.364	0.154	0.005	0.164	0.159	0.136	0.256	0.372	0.214	0.020	0.232													
160Gd	0.777	0.791	0.807	0.898	1.615	1.148	0.253	1.153	0.514	0.795	0.025	0.794	0.776	0.734	1.416	2.033	0.697	0.037	0.902													
163Dy	1.331	1.222	1.518	1.514	2.159	1.608	0.328	1.531	2.108	1.239	0.013	1.303	1.276	1.290	2.081	3.002	0.875	0.099	1.040													
167Er	0.917	0.866	1.122	1.076	1.400	1.029	0.271	0.972	1.225	0.901	0.044	0.873	0.923	0.936	1.302	2.034	0.604	0.080	0.700													
174Yb	0.860	0.818	0.888	0.945	1.208	3.180	3.958	0.834	1.195	0.779	0.005	0.794	0.766	0.893	13.375	1.920	0.629	0.036	0.693													

CIC = coarse grain, isolated, core.

CCC = coarse grain, in clusters, core.

CR = coarse grain rim.

CPR = coarse grain percolative rim.

P = small to medium sized, interstitial or percolative grain.

Pv = percolative veinlet.

Cpxenite = grain in clinopyroxenite patch.

Table 1A (continued)

SP12-7			sp12-10		SP12-12		SP12-12		SP12-12		SP12-12		SP12-13		SP12-13		SP12-13		SP12-14		SP12-14		SP12-14		SP12-16		SP12-16		SP12-16		SP12-16	
CR	CPR		CCC		CCC		CPR		CCC		P		CIC		CIC		CR		CIC		CPR		P						CIC		CR	
n=1	Ave.	±	Ave.	±	Ave.	±	Ave.	±	Ave.	±	n=1	Ave.?	±	Ave.?	±	Ave.?	±	Ave.	±	n=1	n=1	Ave.?	±	Ave.?	±	Ave.?	±	Ave.	±	Ave.	±	
50.90	50.32	0.40	51.29	0.40	51.72	0.11	51.80	0.35	51.60	0.82	52.27	49.88	51.29							50.85	0.15	50.50	51.14	51.40	50.15	50.75	0.40	51.01	0.07			
0.18	0.23	0.03	0.09	0.01	0.11	0.00	0.06	0.03	0.09	0.01	0.08	0.15	0.13							0.10	0.00	0.08	0.09	0.40	0.36	0.29	0.00	0.33	0.02			
5.13	4.44	0.22	5.35	0.45	4.35	0.03	3.44	1.10	4.52	1.17	2.97	5.27	5.07							5.74	0.12	5.81	5.78	4.68	5.46	5.63	0.22	4.53	0.26			
1.47	1.22	0.08	1.32	0.17	1.48	0.12	1.24	0.29	1.48	0.13	1.31	1.26	1.14							1.42	0.01	1.39	1.53	1.29	1.55	1.57	0.02	1.26	0.05			
3.07	2.62	0.01	2.60	0.02	2.42	0.20	2.48	0.14	2.69	0.14	2.55	2.48	2.32							2.81	0.04	2.66	2.57	2.55	2.67	2.76	0.02	2.47	0.10			
0.11	0.12	0.05	0.09	0.04	0.10	0.02	0.12	0.04	0.08	0.03	0.09	0.10	0.07							0.07	0.01	0.10	0.11	0.05	0.04	0.07	0.06	0.09	0.02			
16.42	15.28	0.30	15.51	0.25	16.23	0.35	17.10	0.32	16.60	0.59	16.20	16.09	16.27							15.94	0.24	15.50	15.32	16.31	15.74	15.91	0.43	15.86	0.39			
21.80	22.98	0.20	22.67	0.16	23.15	0.56	22.46	0.74	21.88	0.23	23.67	21.84	22.24							21.81	0.24	22.42	22.43	22.44	22.20	21.69	0.11	22.41	0.50			
0.39	0.35	0.01	0.46	0.03	0.36	0.01	0.36	0.06	0.38	0.02	0.34	0.55	0.48							0.47	0.03	0.52	0.57	0.42	0.56	0.53	0.07	0.45	0.07			
99.48	97.54	0.28	99.38	0.23	99.91	0.03	99.05	0.77	99.36	0.24	99.48	97.62	99.01							99.21	0.08	98.97	99.54	99.54	98.73	99.19	0.93	98.40	0.42			
90.51	91.22	0.20	91.40	0.07	92.28	0.45	92.27	0.03	91.64	0.65	91.88	91.74	92.38							90.99	0.13	91.22	91.39	91.79	91.19	91.11	0.28	91.97	0.47			
16.11	15.52	0.19	14.14	0.58	18.60	1.10	19.62	1.43	18.48	3.33	22.83	13.82	13.10							14.24	0.25	13.85	15.03	15.60	15.99	15.74	0.36	15.72	0.23			
n=1	n=1	n=1	n=1	n=1	n=1	n=1	n=1	n=1	n=1	n=1	n=1	n=1	n=1	n=1	n=1	n=1	n=1	n=1	n=1	n=1	n=1	n=1	n=1	n=1	n=1	n=1	n=1	n=1	n=1	n=1	n=1	
60.2	60.9		60.0		60.0		61.2		55.5		64.5	55.0	56.0	57.0	54.8	64.7	59.7	60.0	55.0	58.0												
983	1005		673		594		710		562		604	843	849	841	535	517	570	2341	2154	1411												
8.04	8.06		16.45		10.38		8.79		4.04		4.11	7.17	5.91	6.94	23.07	17.93	22.13	2.71	2.02	2.86												
5.71	5.78		6.49		6.97		6.93		6.40		7.03	6.91	6.57	6.99	6.04	5.61	6.44	8.42	8.70	7.93												
2.78	3.02		2.06		14.83		16.94		10.78		13.27	4.13	3.73	3.65	1.70	1.72	1.69	4.34	3.99	3.67												
0.316	0.343		1.087		1.793		1.381		1.239		1.078	0.140	0.160	0.080	1.783	1.409	1.923	0.010	0.010	0.038												
1.596	1.434		2.351		7.824		7.062		7.012		5.608	0.540	0.470	0.500	5.127	4.090	5.522	0.280	0.260	0.300												
1.990	1.991		1.213		7.117		6.703		6.491		5.518	0.780	1.130	0.810	3.171	2.553	3.365	1.630	1.550	1.409												
0.639	0.566		0.455		1.472		1.464		1.293		1.254	0.390	0.560	0.580	0.614	0.491	0.646	0.910	1.020	0.893												
0.245	0.202		0.177		0.294		0.297		0.297		0.278	0.240	0.190	0.230	0.178	0.147	0.205	0.470	0.400	0.357												
0.746	0.602		0.748		1.236		1.153		1.062		0.989	0.790	0.780	0.880	0.670	0.599	0.601	1.510	1.490	1.487												
1.022	0.966		0.997		1.167		1.189		1.029		1.138	1.010	1.010	1.390	0.925	0.852	1.033	1.390	1.580	1.434												
0.671	0.691		0.680		0.786		0.830		0.737		0.773	0.780	0.690	0.670	0.712	0.636	0.966	1.160	0.860	0.862												
0.597	0.638		0.701		0.721		0.823		0.675		0.699	0.790	0.880	0.780	0.720	0.678	0.742	1.000	0.920	0.813												

Table 1B
Major and trace element compositions of orthopyroxene cores.

	SP03-10		SP03-12		SP03-15		SP03-19b		SP12-07		SP12-12		SP12-13		SP12-16	
	Ave.	sd	Ave.	sd	Ave.	sd	Ave.	sd	Ave.	sd	Ave.	sd	Ave.	sd	Ave.	sd
SiO ₂	54.43	0.03	54.28	0.38	53.79	1.12	54.28	0.21	54.73	0.23	56.10	0.56	55.02	1.01	55.11	0.13
TiO ₂	0.08	0.00	0.09	0.02	0.08	0.01	0.10	0.02	0.09	0.01	0.03	0.01	0.04	0.01	0.15	0.01
Al ₂ O ₃	4.70	0.25	4.22	0.13	4.47	0.54	3.69	0.28	4.44	0.18	2.35	0.28	4.48	0.11	3.96	0.52
Cr ₂ O ₃	0.88	0.11	0.87	0.03	0.92	0.11	0.94	0.07	0.79	0.14	0.79	0.07	0.87	0.07	0.79	0.18
FeO	5.66	0.11	5.82	0.13	5.65	0.29	7.43	0.08	6.08	0.08	5.76	0.12	6.11	0.02	6.30	0.04
MnO	0.15	0.05	0.12	0.06	0.11	0.03	0.17	0.02	0.20	0.12	0.10	0.01	0.10	0.01	0.12	0.01
MgO	31.72	0.76	32.56	0.32	31.64	1.54	31.63	0.57	32.13	0.16	33.02	0.54	33.40	0.51	33.56	0.04
CaO	1.75	0.17	1.28	0.21	1.92	0.34	1.22	0.06	1.43	0.05	1.31	0.46	0.96	0.00	1.19	0.34
Na ₂ O	0.04	0.02	0.03	0.01	0.04	0.01	0.04	0.02	0.02	0.01	0.02	0.01	0.03	0.01	0.03	0.01
Total	99.40	0.23	99.26	0.46	98.62	2.09	99.59	0.67	99.98	0.41	99.48	0.39	100.98	1.37	101.18	0.24
Mg#	90.90	0.36	90.88	0.11	90.90	0.02	88.36	0.24	90.41	0.11	91.09	0.12	90.70	0.10	90.48	0.06
CR#	11.17	1.76	12.13	0.72	12.07	0.05	14.56	0.51	10.66	1.36	18.37	0.48	11.53	0.59	11.74	1.08
	n = 1		n = 1		n = 3		n = 1		n = 2		n = 1		n = 2		n = 2	
48Ti	409		398		486	61	305		221	14	135		278	7	754	24
88Sr	0.04		3.18		0.24	0.18	0.52		0.22	0.04	0.79		0.27	0.13	0.14	0.05
89Y	1.22		1.71		0.99	0.10	2.22		0.60	0.10	0.80		0.66	0.03	0.79	0.16
90Zr	0.18		0.31		0.22	0.06	0.94		0.38	0.04	1.36		0.51	0.02	0.54	0.02
139La	0.001		0.014		0.007	0.004	0.048		0.008	0.003	0.026		0.001	0.000	0.001	0.000
140Ce	0.002		0.007		0.010	0.008	0.025		0.027	0.002	0.102		0.010	0.000	0.010	0.000
143Nd	0.014		0.020		0.012	0.002	0.019		0.032	0.006	0.107		0.030	0.000	0.025	0.007
147Sm	0.019		0.025		0.012	0.006	0.031		0.013	0.001	0.034		0.201	0.000	0.020	0.000
151Eu	0.011		0.017		0.007	0.002	0.022		0.007	0.001			0.015	0.007	0.010	0.000
160Gd	0.058		0.071		0.039	0.003	0.135		0.026	0.006	0.046		0.065	0.007	0.060	0.000
163Dy	0.138		0.220		0.113	0.022	0.367		0.065	0.000	0.094		0.105	0.049	0.110	0.000
167Er	0.161		0.254		0.139	0.039	0.344		0.069	0.009	0.103		0.095	0.007	0.115	0.007
174Yb	0.248		0.371		0.205	0.043	0.454		0.145	0.004	0.173		0.165	0.007	0.175	0.007

plagioclase and displays a greater enrichment in all the REEs. As for cpx, SP12 orthopyroxene have lower concentrations in HREEs.

REE partition coefficients between ortho- and clinopyroxene depend on the equilibration temperature (Lee et al., 2007). Their patterns give insight into the grain-scale chemical equilibrium (Agranier and Lee, 2007; Witt-Eickschen and O'Neill, 2005). Pyroxene pairs in St. Paul samples are not in equilibrium for the M- and LREEs, as shown by increasing deviation as cationic radii increase, yielding U-shaped curves (Fig. 4A and B). This effect is ascribed to partial equilibration with trapped melts and short equilibration times by Agranier and Lee, 2007. The stronger is the LREE rebound the shorter is the equilibration time.

4.1. Trace element modelling of SP03 peridotites based on clinopyroxene compositions

This sample suite is characterized by LREE-depleted patterns similar to those characterizing “normal” abyssal peridotites. Melting of this mantle portion can be adequately modelled in the conventional way, at least for the less incompatible elements (M- and HREEs, Ti and Y), i.e. near-fractional, non-modal, melting plus some amount of refertilization due to trapping of partially aggregated percolating melts at the end of the melting column (Johnson and Dick, 1992; Hellebrand et al., 2002; Brunelli et al., 2006). Near-fractional melting with $\leq 0.5\%$ residual porosity of a Depleted MORB Mantle source (Depleted MORB Mantle of Workman and Hart, 2005; model parameters from Brunelli et al., 2006) in the spinel stability field reproduces the HREE contents but leaves residues containing twice as much clinopyroxene than that actually measured in the samples, with MREE/HREE ratios too high. The H- to MREEs of the SP03 samples are better reproduced if melting starts in the garnet stability field, which has for effect of over depleting the lighter elements (Johnson et al., 1990; Hellebrand et al., 2002). In order to fit both trace element patterns in clinopyroxene and modal mineral proportions of the SP03 samples it is necessary to consider some amount of refertilization by trapped melts. Percolation and retention of partial melts at the top of the melting column followed by their freezing when mantle enters

the conductive thermal boundary layer may account for small changes in the most incompatible element compositions and in the residual modes through opx dissolution and $Cpx \pm Ol \pm Sp \pm Pl$ crystallization (Kelemen et al., 1995; Hellebrand et al., 2002; Seyler et al., 2001).

SP03 REE patterns show a subparallel shift from the depleted-most to the enriched-most clinopyroxenes (Fig. 4A), a feature incompatible with partial melting fractionation which steepens REE pattern slopes as melting extent increases. We interpret this variation as result of modal refertilization due to trapping of partially aggregated percolating melts as described in Brunelli et al. (2006). These melts are expected to be close to equilibrium with the residue and significantly different from MORB-like (e.g., fully aggregated) melts; furthermore, their crystallization gives new minerals in equilibrium with the residual assemblage.

Accordingly, we model the SP03 samples by 14% partial melting starting in the garnet stability field up to 4% followed by 10% in the spinel stability field, with 0.5% residual porosity over the whole melting column. In order to match the observed patterns, however, then requires addition of 1–3 to 3.3% of a partially aggregated melt extracted over the previous melting interval (7–13%) in the spinel stability field (Fig. 5; Table 2).

The resulting clinopyroxene proportion varies from 3.2 to 4.5% in good agreement with the observed modal distribution (4.0 ± 1.1 vol.%) and textures. The expected compositional range is reported in Fig. 4A as blue field. A minor misfit has to be accounted for the most light elements. La and Ce of the measured clinopyroxene show a weak enrichment with respect to the model patterns (Fig. 4A). This behaviour, common in abyssal peridotite, can be accounted for by local chromatographic enrichment due to percolation of MORB-like melts (Suh et al., 1998).

Melting starting in the garnet stability field also accounts for the weak negative Sr anomaly present in all the measured patterns. In fact the preferential partitioning of Sr into clinopyroxene and the higher melting coefficient of this phase with respect to garnet (Walter, 1998) results in a weak negative Sr anomaly in residual spinel field equilibrated clinopyroxene. If any plagioclase would have crystallized during late-stage events a strong negative Sr anomaly would appear in the associated clinopyroxene after equilibration. Lack of this

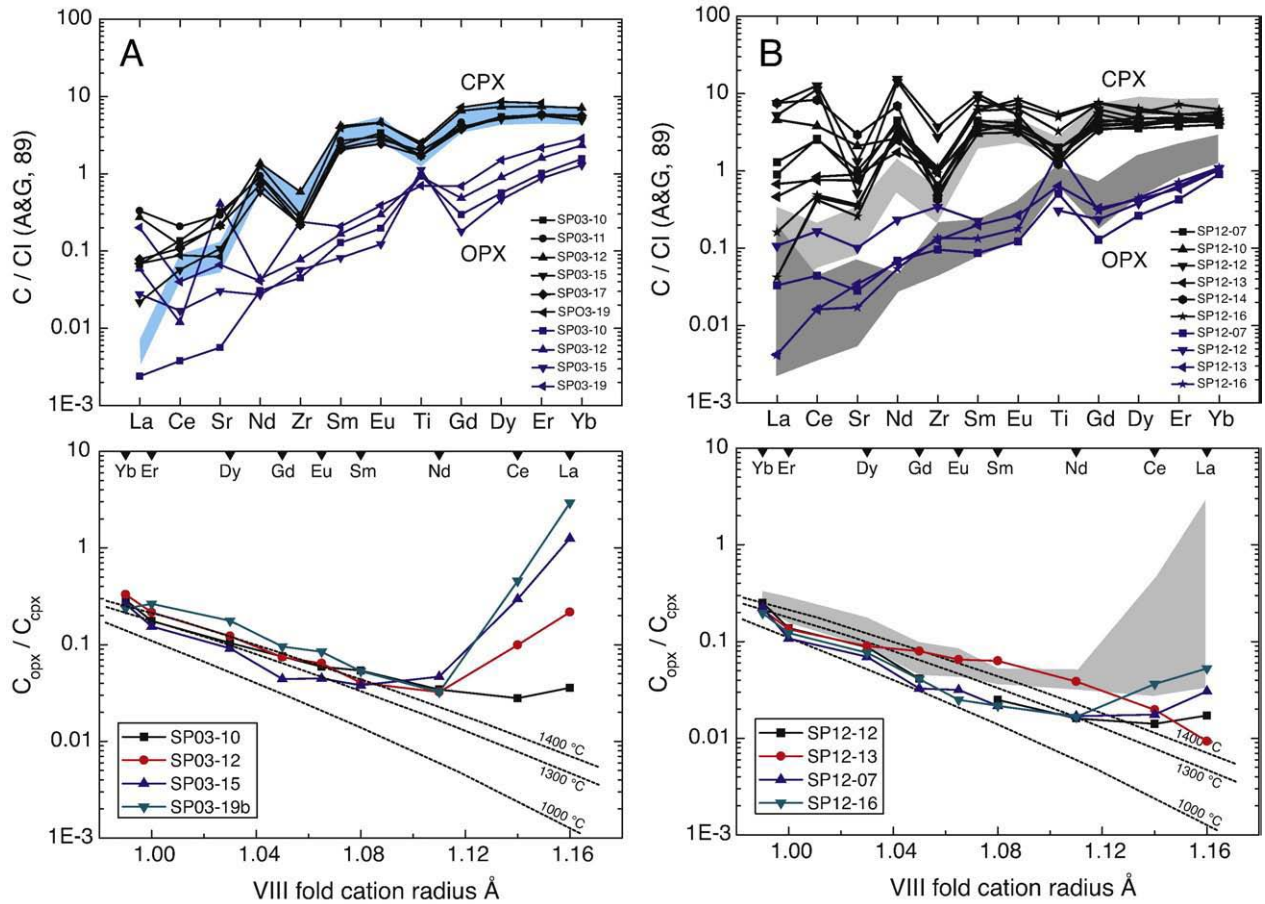


Fig. 4. A: Upper panel: Chondrite-normalized REE contents in Cpx and Opx cores for six peridotite samples from St. Paul dive SP03 (CI from: [Anders and Grevesse, 1989](#)). The blue field represents the compositional range expected for a residual cpx in a 14% (4% grt + 10% sp) molten MORB mantle source ([Workman and Hart, 2005](#)) refertilized by a variable proportions (1.3–3.3 vol.%) of a partially aggregated melt as discussed in the text. Lower panel: REE partitioning between Opx and Cpx for four peridotites plotted against VIII-fold cationic radius. Dashed lines correspond to the equilibrium partitioning trends at different temperatures according to [Agranier and Lee \(2007\)](#). B: Upper panel: Chondrite-normalized REE contents in Cpx and Opx cores for five peridotite samples from St. Paul dive SP12 (CI from: [Anders and Grevesse, 1989](#)). The grey fields show the compositional variation of the Opx and Cpx in SP03 peridotites. Lower panel: REE partitioning between Opx and Cpx for four peridotites plotted against VIII-fold cationic radius. Dashed lines correspond to the equilibrium partitioning trends at different temperatures according to [Agranier and Lee \(2007\)](#). The grey field correspond to SP03 samples.

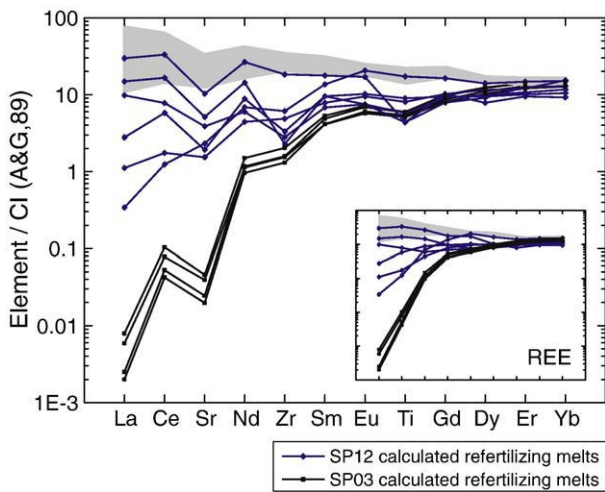


Fig. 5. Calculated composition of the trapped percolating melts in samples SP03 (black solid lines) and SP12 (blues solid line) following the method of [Brunelli et al., 2006](#). The grey field shows the compositional range of the basalts and alkali basalts sampled in the St. Paul region ([Melson et al., 1972](#); [Hekinian et al., 2000](#)). The REE restricted pattern is reported in the small inset. SP12 patterns are interpreted as result of mixing between chromatographic-modified alkaline melts and partially aggregated depleted MORB melts.

fingerprint argues against equilibration of the clinopyroxene cores in the plagioclase field, even when plagioclase is present in the rock (sample SP03-11). On the contrary the simple crystallization of Cpx (\pm Sp, Opx, and Ol) during the late percolation would gently mask the garnet effect by rising the Sr/Sr* [$Sr^* = (Ce \cdot Nd)^{1/2}$] because of the major incompatibility of Sr with respect to Nd in clinopyroxene. Three samples show evidence for late-stage melt percolation that have crystallized Cpx + Sp (SP03-12) or Cpx + Pl (SP03-11 and SP03-19). These clinopyroxenes are in equilibrium with depleted partially aggregated melts apart the sample SP03-11 that is possibly equilibrated with a fully aggregated MORB (blue lines in [Fig. 4A](#)).

4.2. Trace element modelling of SP12 peridotites based on clinopyroxene compositions

SP12 peridotites differ from SP03 and from most abyssal peridotites by their sensible enrichments in LREEs and other incompatible elements (Ba, Sr and Zr). Their REE patterns are highly variable and indicative of a complex geochemical history ([Fig. 4B](#)). They cannot be connected to each other either by varying the extent of melting or by considering variable amounts of refertilization by partially aggregated melts from a Depleted MORB Mantle source. Therefore, the difference between samples SP03 and SP12 has to be found in a metasomatic process caused by infiltration of a melt in, and

Table 2
Calculated melt composition (ppm) for percolating/trapped melts in the SP03 and SP12 sample suites.

	SP03-10	SP03-11	SP03-12	SP03-15	SP03-17	SP03-19	SP12-07	SP12-12	SP12-13	SP12-14	SP12-16	SP12-10
La	0.002	0.0005	0.002	0.001	0.001	0.0005	0.65	7.00	0.26	3.50	0.08	2.30
Ce	0.06	0.03	0.06	0.05	0.03	0.03	3.50	20.00	1.05	10.00	0.75	4.70
Sr	0.36	0.15	0.36	0.31	0.19	0.15	15.0	80.0	12.0	40.0	18.0	30.0
Nd	0.68	0.43	0.68	0.51	0.53	0.43	4.0	12.0	2.0	6.5	3.1	2.7
Zr	8.0	5.2	8.0	6.0	6.2	5.2	13.0	72.0	19.2	9.0	24.0	11.0
Sm	0.78	0.61	0.78	0.60	0.71	0.61	1.4	2.6	1.2	1.4	2.0	1.0
Eu	0.40	0.34	0.40	0.32	0.39	0.34	0.57	0.95	0.53	0.42	1.15	0.42
Ti	2599	2356	2599	2220	2560	2356	3900	1900	3500	1900	7500	2500
Gd	1.95	1.70	1.95	1.59	1.90	1.70	1.85	2.00	2.00	1.55	3.20	1.80
Dy	3.01	2.68	3.01	2.50	2.96	2.68	2.30	1.90	2.80	2.20	3.40	2.40
Er	2.26	2.05	2.26	1.92	2.23	2.05	1.60	1.50	1.90	2.00	2.35	1.70
Yb	2.39	2.19	2.39	2.06	2.36	2.19	1.70	1.50	2.50	2.10	2.45	1.90

subsequent reaction with, a peridotite matrix. The complexity of the REE patterns suggests fractionation by chromatography, a process able to strongly fractionate the REEs in migrating melts and reacted peridotite (Navon and Stolper, 1987; Bodinier et al., 1990).

Percolation of large volumes of melt often produces pyroxene-poor harzburgite or dunite due to pyroxene dissolution by a decompressing melt (Kelemen et al., 1995 and references therein), a feature not observed in SP12 textures and modes. Rather, the textural similarity of the SP12 and SP03 peridotites indicates that mineral reactions, such as orthopyroxene dissolution/corrosion and $Ol + Cpx + Sp \pm Pl$ crystallization, are as limited as they are in SP03 peridotites. Modal refertilization appears to have been small, implying that the sampled peridotites were not a significant pathway for melt migration. So, explaining the greatest enrichment in incompatible elements observed in SP12 clinopyroxenes may require a model involving simple ion exchange reaction between a basaltic magma (e.g., fully aggregated melts) and residual peridotite without reaction involving significant production or consumption of mineral phases, and not only element exchange, as proposed by Bodinier et al. (1990).

The close similarity of major element composition and textural appearance of SP03 and SP12 samples allow us assume that the two suites differ largely in the composition of the melt(s) that percolated in the last asthenospheric events and not in the main stage of decompressional partial melting. Even under the limits of this assumption we have here the chance to estimate the composition of the metasomatizing liquids by assuming that the two protoliths underwent similar partial melting histories leading to a similar major and trace element residual compositions at the end of the melting process prior to melt impregnation. If we assume a similar thermal setting and theoretical porosity profile for SP03 and SP12 mantle parcels, trapping and equilibrating the same amount of liquid in SP12 samples as in SP03 samples (average 2.1 wt.%), we can estimate the composition of the liquid necessary to obtain the observed clinopyroxene patterns. We have therefore calculated the composition of a hypothetical liquid trapped in a partially melted ($F = 14\%$) source necessary to fit the measured pattern. Plagioclase or clinopyroxene have been considered to crystallize according to the measured mode. The calculated melt compositions, reported in Table 2 and Fig. 5, fall in between the composition of the alkali basalts sampled near St. Paul Rocks massif (Melson et al., 1972) and the depleted compositions of the partially aggregated melts that were retained in the SP03 samples at the top of the melting region (calculated according to Brunelli et al., 2006). The U- and S-shaped REE patterns of the calculated melts suggest they experienced some amount of chromatographic fractionation before being trapped in the residual peridotite. However, the overall content is easily fitted by simple mixing of the enriched-most alkali basalt erupted in the region and the depleted partially aggregated melts.

SP12 peridotites were sampled on the flank of the St. Peter and Paul Rocks massif close to a major shear zone (about 16 km) that represents a fossil channel through which alkali basaltic magma

travelled (Hekinian et al., 2000; Fig. 1). This type of magma is a possible source for a metasomatic agent.

5. Discussion

5.1. Suboceanic versus subcontinental mantle

SP12 peridotites, sampled on the immersed flank of the St. Peter and Paul Rocks massif, cannot be readily distinguished from the intra-transform ridge SP03 peridotites on the basis of their textures, modes and mineral major element compositions. Both peridotite suites have coarse, nearly undeformed textures alike those that characterize subaxial residual mantle that cooled at depth after upwelling and partial melting. The mineral proportions and major element compositions of the PI-free samples are within the abyssal peridotite spectrum, in between the least (Romanche fracture zone, Seyler and Bonatti, 1997 and Tartarotti et al., 2002) and the most depleted ($15^\circ 20' N$ fracture zone, Seyler et al., 2007) compositions of the Mid Atlantic Ridge. In both locations, the proportion of PI-bearing samples relative to PI-free samples (30:70) is similar to the proportion retrieved in other mid-oceanic regions where PI-free and PI-bearing peridotites occur together (Dick, 1989).

The interpretation of the St. Paul ultramafic mylonites as fragments of subcontinental lithospheric mantle left behind during the opening of the Central Atlantic (Bonatti, 1990) relied on the high jadeite content of the clinopyroxene relicts, low equilibrium temperature of Opx–Cpx pairs, and bulk rock normalized REE patterns decreasing from the LREEs to the HREEs. Our study shows that these features are not found in peridotites sampled at distance from the mylonitic zone (SP03 is about 370 km east of SP12). The alkali-rich compositions of the St. Paul's mylonites result from coeval deformation and recrystallization of a mixture of residual peridotite and alkaline mafics, and this suggests that the mylonite band was, before closure, a major pathway for the alkali basalts. As shown by Hekinian et al. (2000), only the northern border of the St. Peter and Paul Rocks massif was strongly tectonized. In contrast, the southern domain of the ridge, where SP12 peridotites were sampled, underwent less shearing, the deformation being concentrated in narrower and less closely spaced mylonitic zones, permitting the preservation of undeformed peridotites.

The structure of the St. Paul's ridge with its islets of hard, fine-grained mylonites that resisted erosion and serpentinization, is quite similar to the structure of the alpine-type Tinaquillo peridotite massif, which is limited on one side by hills of mylonites intruded by gabbroic sills and on the other side by low-lying serpentinized, undeformed rocks (Seyler et al., 1998).

5.2. Partial melting, refertilization and geodynamic setting

The overall trace element patterns of the clinopyroxenes from site SP03 are reproduced by about 14% near-fractional melting of a MORB

source, starting in the garnet stability field. This conclusion is in agreement with their major element compositions falling in the middle part of the abyssal peridotite compositional field (Hellebrand et al., 2001, 2002; Brunelli et al., 2003, 2006). A similar partial melting scenario and extent are inferred for site SP12 peridotites based on their textures and major element compositions. Such an extent of melting may seem too high for a region interpreted as a cold spot and where very fertile abyssal peridotites have been retrieved (Bonatti et al., 1993). Moreover, a cold conductive thermal regime, due to the edge effect of the numerous closely-spaced transform faults on mantle upwelling would be expected to further inhibit melting by cooling from above, leading to the formation of a thick subaxial lithospheric mantle (Bonatti et al., 2001a,b). A plausible explanation is to consider that the upper mantle already experienced some amount of melt extraction during an ancient partial melting event before rising beneath the modern ridge. This is suggested by Os model age of 0.56 to 1.1 Ga of some St. Paul's samples (Esperança et al., 1999) and the inferred presence of a fossil detached subducted slab beneath the Equatorial Atlantic (Maia et al., 2001; Sichel et al., 2008). In the latter case, there will be a link between old mantle, fertile compositional heterogeneities and production of E- to N-MORBs and alkali basalts during low-degree decompressional partial melting.

To account for LREE enrichments, orthopyroxene dissolution and clinopyroxene crystallization, we invoke reaction with partial melts aggregated over the upper part (spinel field) of the melting region, followed by their trapping as the mantle entered the conductive thermal layer. Although this process has been shown to generally occur beneath the spreading ridges, the calculated amount of melt retention (~2.1%) appears large with respect to that modelled for residual mantle peridotites sampled in "normal" thermal settings of the mid ocean ridge. For instance, melt retention in peridotites from the Vema Lithospheric Section is estimated to be <1% (Brunelli et al., 2006). The larger melt retention can be explained by the colder lithospheric gradient in the St. Paul's region that results in a forced crystallization of the transient melts with reduction of the extracted fluid portion at the end of the melting region. Large sectors of the equatorial Mid Atlantic Ridge between the St. Paul and Romanche FZ are made of variably impregnated mantle rocks, intercalated with gabbroic bodies, usually not covered by an extrusive sequence (Bonatti et al., 1996; Bonatti et al., 2001a,b; Tartarotti et al., 2002, and references therein). The presence of nearly amagmatic crustal emplacement associated with alkali (and water) rich basalts have been ascribed to the superposition of the equatorial Atlantic thermal minimum with the enhanced cold edge effect due to the large age contrasts characterizing this stretch of MAR (Bonatti et al., 2001a,b; Ligi et al., 2005). A similar juxtaposition of alkaline basalts adjacent to amagmatic segments has been reported between 9° and 16°E on the SW Indian Ridge ascribing it to the influence of a thickened lithospheric lid due to ultraslow oblique spreading (Standish et al., 2008).

We ascribe the presence of plagioclase in St. Paul's peridotites to interaction between percolating melts with residual solid. The melt fractions that did not escape the peridotite when the mantle entered the conductive boundary layer crystallized interstitially to form $(Ol +) Cpx + Sp \pm Pl$. Textures clearly show that late-stage percolative clinopyroxene, is associated with Al-rich spinel in Sp-peridotites and with Cr-rich Sp + Pl in Pl-peridotites (Supplementary Fig. 1). In both types of peridotites, the percolating melts were in slight disequilibrium with the coarse-grained mineral assemblages. In Sp-peridotites melt–rock reactions caused orthopyroxene dissolution associated with complex Al–Cr exchange reactions between melt, pyroxenes and spinel, often leading to the formation of small Sp–Px symplectites (Seyler et al., 2007; Suhr et al., 2008). In the Sp + Pl stability field, a major effect of this disequilibrium is to decrease Al relative to Cr in orthopyroxene, clinopyroxene and spinel as shown by Dick (1989) and to generate Sr and Eu depletions in the clinopyroxene. In most of the samples in this study, the residual phases

did not fully re-equilibrate, except for a few rims, so depleted trace element patterns derived from partial melting have been preserved. Both interstitial paragenesis appear to have crystallized in similar conditions of P and T (e.g., in the thermal boundary layer), so we speculate that variations in melt chemistry, oxygen fugacity and/or other thermodynamic variables were the true factors controlling plagioclase or spinel crystallization instead of pressure. Pl-bearing abyssal peridotites have been retrieved only at cold and/or ultra-slow spreading mid oceanic ridges. Because of the reduced melt production a cold mantle environment allows preserving source heterogeneities as variable composition of the melt that percolate upward through the partially molten peridotite.

5.3. Alkaline melt percolation and related metasomatism in St. Peter and Paul Rocks peridotites

Trace element distribution in the SP12 clinopyroxenes attest for local equilibration with enriched melts compositionally akin to the basalts erupted in the St. Paul region. On the other hand, major element compositions of the SP12 peridotites are very similar to those characterizing the SP03 peridotites, typical of the residues of normal decompressional partial melting that led to MORB generation. It is thus unlikely that the SP12 peridotites represent the residues of the source of the alkali basalts. The compositions of the calculated impregnating melts fall in between the field of the St. Paul and Romanche MORBs and alkali MORBs (Melson et al., 1972; Hekinian et al., 2000; Ligi et al., 2005) and the depleted partially aggregated melts percolating through the mantle at the top of the melting region (Fig. 5). Without going into details of the genesis of these melts we can stress that they could derive from mixing true alkali basalts with depleted partially aggregated MORB components or they represent the primitive melts of the erupted alkali basalts prior shallow level fractional crystallization. Their enriched character suggests either the presence of low-degree melt components from a garnet bearing source or an enriched source.

Two important questions concern the timing of the metasomatic event and the spatial relationships between the source of the metasomatizing melts and the SP12 sample domain. In those samples where the compositional variability was investigated (core–rim analyses, porphyroclasts versus percolative clinopyroxene), lack of clinopyroxene zoning and lack of significant texture-related variations in the trace element contents (except in Pl-bearing samples) indicate that the SP12 peridotites were well equilibrated at the grain to the sample (e.g., 10 to 100 cm) scales. At the same time trace element compositions strongly vary from sample to sample. These observations suggest that the metasomatism occurred at high temperature in a hot peridotite matrix, in which melts may infiltrate for relatively long distances without solidifying. They also suggest short-scale heterogeneities and small melt volumes. In this scenario separate batches of percolating melts may have experienced chromatographic fractionation without significantly homogenizing. Finally, relations between textures and grain compositions indicate that the metasomatic melts froze at the base of the lithosphere. Overall these characters are representative of the top of the asthenospheric region.

Chromatographic effects vary as a function of distance from the source of the metasomatizing melt (Navon and Stolper, 1987). Unfortunately, our sampling cannot help to understand the exact location of this source and its spatial relationships with each sample. As indicated by the pyroxene-rich SP12 peridotites, the SP12 sample domain was not a pathway for the melt extraction. Rather, their location close to the SPPR alkaline mylonites strongly suggests that this mantle parcel might have been infiltrated by alkalic melts escaped from melt channels now homogenized in the mylonitic band. Enriched and "normal" melts from the host depleted mantle may have variably mixed during upwelling or after being focused and reacted in an anastomosing pathway. In this scenario, the peridotites (SP12) represent

parcels of the residual host that were located in between the channels. The percolating melt, responsible for the observed enrichment, was the melt flowing-out from the channels after melt–rock interaction, that explains the inflections observed in the calculated REE patterns.

6. Conclusions

Mantle peridotites from the St. Peter and Paul region of the equatorial Atlantic show that some mantle batches can be infiltrated by and partially equilibrated with alkaline basalts similar to those frequently erupted in this region. The metasomatized mantle parcels mimic in their composition a subcontinental mantle.

The particular cold mantle environment allows preservation of source heterogeneities as variable composition of the extracted melts whereas in more normal thermal settings these heterogeneities may be diluted and smoothed out by the enhanced melting of the host Depleted MORB Mantle-type mantle source and the associated asthenospheric melt flux. This results in the eruption of alkali basalts together with normal MORB in the same region.

Acknowledgments

We thank T. Juteau and R. Hekinian for providing samples and initiating this work. We are grateful to H. Dick and an anonymous reviewer for the careful review and the interesting discussion that greatly improved the manuscript. We are grateful to B. Boyer for assistance with the trace element analyses at the ion microprobe facility of Montpellier, M. Fialin and F. Couffignal for the analytical assistance at Camparis, IGP, Paris, and L. Ottolini for the analyses at CNR-IGG, Pavia. We thank M. Ligi (ISMAR-CNR, Bologna) and E. Bonatti (LDEO-Columbia, NY) for providing the detailed bathymetric data. MS has been supported by INSU DyETI program and fund from the Laboratoire de Géosciences Marines (IPG Paris), DB has been supported by COFIN-PRIN 2007.

Appendix A. Supplementary data

Fig. 1 A): SP12-16 thin section (harzburgite; 4×4 cm) representative of the coarse-granular texture of SP12 rocks and their high degree of alteration. B): Coarse spinel (Sp) surrounded by clinopyroxene (Cpx) in serpentine (former olivine) matrix. The cpx border contains spinel intergrowths. On the right side, another interstitial clinopyroxene rims (serpentinized) orthopyroxene (Opx). Sample SP03-15. C): Clinopyroxene crystal (Cpx) interstitial between (serpentinized) olivine (Ol) and (partially serpentinized) orthopyroxene (Opx). The Cpx crystal also fills a corrosion path within the Opx porphyroclast. Sample SP03-12. D): Late-stage spinel (Sp), plagioclase (Pl) and clinopyroxene (Cpx) crystallized within serpentine matrix (top), at the tip of a clinopyroxene porphyroclast (Cpx) and between two porphyroclasts of serpentinized orthopyroxene (Opx) and clinopyroxene. The spinel patches (top) are aggregates of several, subhedral grains. Sample SP12-16. The scale bar is 0.2 mm. False colours are used to highlight mineral species and textures in microphotos B–D.

Fig. 2. Composition of orthopyroxene cores from St. Paul peridotites, Sites SP03 and SP12. (A) Plagioclase-free, spinel peridotites. (B) Plagioclase-bearing, spinel peridotites. Thin section containing the clinopyroxene patch (SP03-19b) is distinguished.

Fig. 3. Composition of spinels from St. Paul peridotites, Sites SP03 and SP12. Gray fields represent spinels from plagioclase-free abyssal peridotites; 80% of these compositions fall in the high density field (dark gray). Spinels from plagioclase-bearing, spinel peridotites evolve along trends of increasing Cr# and TiO₂, caused by MORB–peridotite interaction at low pressure.

Note: The supplementary material accompanying this article is available at doi:10.1016/j.epsl.2009.11.028.

References

- Agranier, A., Lee, C.-T.A., 2007. Quantifying trace element disequilibria in mantle xenoliths and abyssal peridotites. *Earth Planet. Sci. Lett.* 257, 290–298.
- Anders, E., Grevesse, N., 1989. Abundances of the elements: meteoritic and solar. *Geochim. Cosmochim. Acta* 53, 197.
- Bodinier, J.-L., Vasseur, G., Vernières, J., Dupuy, C., Fabriès, J., 1990. Mechanism of mantle metasomatism: geochemical evidence from the Lherz orogenic peridotite. *J. Petrol.* 31, 597–628.
- Bonatti, E., 1990. Subcontinental mantle exposed in the Atlantic Ocean on St. Peter–Paul islets. *Nature* 345, 800–802.
- Bonatti, E., Brunelli, D., Fabretti, P., Ligi, M., Portaro, R., Seyler, M., 2001a. Steady-state creation of crust-free lithosphere at cold spots in mid-ocean ridges. *Geology* 29, 979–982.
- Bonatti, E., Brunelli, D., Fabretti, P., Ligi, M., Portaro, R., Seyler, M., 2001b. Steady-state creation of crust-free lithosphere at cold spots in mid-ocean ridges. *Geology* 29, 979–982.
- Bonatti, E., Ligi, M., Carrara, G., Gasperini, L., Turko, N., Perfiliev, A., Peyve, A., Sciuto, P.F., 1996. Diffuse impact of the Mid Atlantic Ridge with the Romanche transform: an ultracold ridge/transform intersection. *J. Geophys. Res.* 101, 8043–8054.
- Bonatti, E., Seyler, M., Sushevskaya, N., 1993. A cold suboceanic mantle belt at the Earth's equator. *Science* 261, 315–320.
- Bottazzi, P., Ottolini, L., Vannucci, R., Zanetti, A., 1994. An accurate procedure for the quantification of rare elements in silicates. *Proc. of the Ninth International Conference on Secondary Ion Mass Spectrometry SIMS IX*. John Wiley & Sons, New York, pp. 927–930.
- Brey, G.P., Kohler, T., 1990. Geothermobarometry in 4-phase lherzolites. 2. New thermobarometers and practical assessment of existing thermobarometers. *J. Petrol.* 31, 1353–1378.
- Brunelli, D., Cipriani, A., Ottolini, L., Peyve, A., Bonatti, E., 2003. Mantle peridotites from the Bouvet Triple Junction Region, South Atlantic. *Terra Nova* 15 (3), 194–203. doi:10.1046/j.1365-3121.2003.00482.x.
- Brunelli, D., Seyler, M., Cipriani, A., Ottolini, L., Bonatti, E., 2006. Discontinuous melt extraction and weak refertilization of mantle peridotites at the Vema Lithospheric Section (Mid-Atlantic Ridge). *J. Petrol.* 47, 745–771.
- Darwin, C., 1891. Geological observations on the volcanic islands and parts of South America visited during the voyage of HMS Beagle, London, 3rd Ed.
- Dick, H.J.B., 1989. Abyssal peridotites, very slow spreading ridges and ocean ridge magmatism. In: Saunders, A.D., Morris, M.J. (Eds.), *Magmatism in the ocean basins: Geol. Soc. Spec. Publ. London*, vol. 42, pp. 71–105.
- Esperança, S., Sichel, S.E., Horan, M.F., Walker, R.J., Juteau, T., Hekinian, R., 1999. Some Abyssal Peridotites Are Old! Ninth Annual V. M. Goldschmidt Conference, August 22–27, Abs. No. 7389.
- Frey, F.A., 1970. Rare earth and potassium abundances in St. Paul's Rocks. *Earth Planet. Sci. Lett.* 7, 351–360.
- Gasperini, L., Bonatti, E., Brunelli, D., Carrara, G., Cipriani, A., Fabretti, P., Gilod, D., Ligi, M., Peyve, A., Skolotnev, S., Susini, S., Tartarotti, P., Turko, N., 1997. New data on the geology of the Romanche F.Z., equatorial Atlantic: PRIMAR-96 cruise report. *Giornale di Geol.* 59/1–2, 3–18.
- Hekinian, R., Juteau, T., Gracia, E., Udintsev, G., Sichel, B., Sichel, S.E., Apprioual, R., Ligi, M., 2000. Submersible observations of Equatorial Atlantic Mantle: The St. Paul Fracture Zone region. *Mar. Geoph. Res.* 21, 529–560.
- Hellebrand, E., Snow, J.E., Hoppe, P., Hofman, A.W., 2002. Garnet-field melting and late-stage refertilization in 'residual' abyssal peridotites from the Central Indian Ridge. *J. Petrol.* 43, 2305–2338.
- Hellebrand, E., Snow, J.E., Dick, H.J.B., Hofmann, A.W., 2001. Coupled major and trace-element melting indicators in mid-ocean ridge peridotites. *Nature* 410, 677–681.
- Hellebrand, E., Snow, J.E., Mostefaoui, S., Hoppe, P., 2005. Trace element distribution between orthopyroxene and clinopyroxene in peridotites from the Gakkal Ridge: a SIMS and NanoSIMS study. *Contrib. Mineral. Petrol.* 150, 486–504.
- Johnson, K.T.M., Dick, H.J.B., 1992. Open system melting and spatial variation of peridotite and basalt at the Atlantis II Fracture Zone. *J. Geophys. Res.* 97, 9219–9241.
- Johnson, K.T.M., Dick, H.J.B., Shimizu, N., 1990. Melting in the oceanic upper mantle: an ion microprobe study of diopsides in abyssal peridotites. *J. Geophys. Res.* 95, 2661–2678.
- Kelemen, P.B., Shimizu, N., Salters, V.J.M., 1995. Extraction of mid-ocean ridge basalt from the upwelling mantle by focused flow of melt in dunite channels. *Nature* 375, 747–753.
- Lee, C.-T.A., Harbert, A., Leeman, W.P., 2007. Extension of lattice strain theory to mineral/mineral rare earth element partitioning: an approach for assessing disequilibrium and developing internally consistent partition coefficients between olivine, orthopyroxene, clinopyroxene and basaltic melt. *Geochim. Cosmochim. Acta* 71, 481–496.
- Ligi, M., Bonatti, E., Cipriani, A., Ottolini, L., 2005. Water-rich basalts at mid-oceanic ridge cold spots. *Nature* 434, 66–69.
- Maia, M., Sichel, S., Esperança, S., Thiriot, J.-L., 2001. The Equatorial Atlantic "cold spot": constraints from osmium isotopes, plate kinematics and tomography, EUG XI. *J. Conf. Abstr.* 6, 1.
- Melson, W.G., Hart, S.R., Thompson, G., 1972. St. Paul's Rocks, equatorial Atlantic: petrogenesis, radiometric ages and implications on sea floor spreading. *Mem. Geol. Soc. Am.* 132, 241–272.
- Melson, W.G., Jarosewich, E., Bowen, V.T., Thompson, G., 1967a. St. Peter and St. Paul's Rocks: a high temperature mantle-derived intrusion. *Science* 155, 1532–1535.
- Melson, W.G., Jarosewich, E., Cifelli, R., Thompson, G., 1967b. Alkali olivine basalt dredged near St-Paul's Rocks, Mid-Atlantic Ridge. *Nature* 215, 381–382.
- Navon, O., Stolper, E., 1987. Geochemical consequences of melt percolation: the upper mantle as a chromatographic column. *J. Geol.* 95, 285–307.

- Roden, M.K., Hart, S.R., Frey, S.H., Thompson, G., 1984. Sr, Nd and Pb isotopic and REE geochemistry of St Paul's Rocks: the metamorphic and metasomatic development of an alkali basalt mantle. *Contrib. Miner. Petrol.* 85, 376–390.
- Sandwell, D.T., Smith, W.H.F., 1997. Marine gravity anomaly from Geosat and ERS1 satellite altimetry. *J. Geophys. Res.* 102, 10039–10054.
- Schilling, J.G., 1987. Cruise Report, R.V. Conrad 28-06. Univ. Rhode Island, pp. 1–16.
- Schilling, J.G., Ruppel, C., Davis, A.N., McCully, B., Tghe, S.A., Kingsley, R.H., Lin, J., 1995. Thermal structure of the mantle beneath the equatorial Mid-Atlantic Ridge: inference from the spatial variation of dredged basalt glass compositions. *J. Geophys. Res.* 100, 10057–10076.
- Seyler, M., Bonatti, E., 1997. Regional-scale melt–rock interaction in Iherzolitic mantle in the Romanche fracture Zone (Atlantic Ocean). *Earth Planet. Sci. Lett.* 146, 273–287.
- Seyler, M., Lorand, J.-P., Dick, H.J.B., Drouin, M., 2007. Pervasive melt percolation reactions in ultra-depleted refractory harzburgites at the Mid-Atlantic Ridge, 15°20'N: ODP Hole 1274. *Contrib. Miner. Petrol.* 153, 303–319.
- Seyler, M., Paquette, J.L., Ceuleneer, G., Kienast, J.R., Loubet, M., 1998. Magmatic underplating, metamorphic evolution and ductile shearing in a Mesozoic lower crustal–upper mantle unit (Tinaquillo, Venezuela) of the Caribbean belt. *J. Geol.* 106, 35–58.
- Seyler, M., Toplis, M., Lorand, J.P., Luguët, A., Cannat, M., 2001. Clinopyroxene microtextures reveal incompletely extracted melts in abyssal peridotites. *Geology* 29, 155–158.
- Sichel, S.E., Esperança, S., Motoki, A., Maia, M., Horan, M.F., Sztamari, P., da Costa, Alves E., Mello, S.L.M., 2008. Geophysical and geochemical evidence for cold upper mantle beneath the equatorial Atlantic ocean. *Braz. J. Geophys.* 26, 69–86.
- Standish, J.J., Dick, H.J.B., Michael, P.J., Melson, W.G., O'Hearn, T., 2008. MORB generation beneath the ultraslow-spreading Southwest Indian Ridge (9°–25°E): major element chemistry and the importance of process versus source. *Geochem. Geoph. Geosyst.* 9, 39. doi:10.1029/2008GC001959.
- Suhr, G., Kelemen, P., Paulik, H., 2008. Microstructures in Hole 1274A peridotites, ODP Leg 209, Mid-Atlantic Ridge: tracking the fate of melts percolating in peridotite as the lithosphere is intercepted. *Geochem. Geoph. Geosyst.* 9 (3), 23. Doi: 10.129/2007GC001726.
- Suhr, G., Seck, H.A., Shimizu, N., Günther, D., Jenner, G., 1998. Infiltration of refractory melts into the lowermost oceanic crust: evidence from dunite- and gabbro-hosted clinopyroxenes in the Bay of Islands Ophiolite. *Contrib. Min. Pet.* 131, 136–154.
- Tartarotti, P., Susini, S., Nimis, P., Ottolini, L., 2002. Melt migration in the upper mantle along the Romanche Fracture Zone (Equatorial Atlantic). *Lithos* 63, 125–149.
- Tilley, C.E., 1947. Dunite mylonites of St-Paul's Rocks (Atlantic). *Am. J. Sci.* 245, 483–491.
- Witt-Eickchen, G., O'Neill, H.S.C., 2005. The effect of temperature on the equilibrium distribution of trace elements between clinopyroxene, orthopyroxene, olivine and spinel in upper mantle peridotite. *Chem. Geol.* 221, 65–101.
- Walter, M.J., 1998. Melting of garnet peridotite and the origin of komatiite and depleted lithosphere. *J. Petrol.* 39, 29–60.
- Workman, R.K., Hart, S.R., 2005. Major and trace element composition of the Depleted MORB Mantle (DMM). *Earth Planet. Sci. Lett.* 231, 53–72.